Shape Optimization Methodology for Reducing the Sonic Boom Initial Pressure Rise

Charbel Farhat*
Stanford University, Stanford, California 94305-3035
Kurt Maute[†] and Brian Argrow[‡]
University of Colorado, Boulder, Colorado 80309-0429
and
Melike Nikbay[§]
Istanbul Technical University, 34469, Ayazaga, Istanbul, Turkey

DOI: 10.2514/1.27607

A shape optimization methodology for reducing the initial shock pressure rise on the ground of a supersonic aircraft is presented. This methodology combines elements from the linearized aerodynamic theory, such as the Whitham F function, with elements from the nonlinear aerodynamic theory, such as the prediction of lift distribution by an Euler or a Navier–Stokes flow solver. It is applied to the optimization of two different airplane concepts developed by Reno Aeronautical and Lockheed Martin, respectively, for the Defense Advanced Research Projects Agency's Quiet Supersonic Platform program. For Reno Aeronautical's laminar-flow supersonic aircraft, the initial shock pressure rise on the ground is reduced by a factor close to 2, from 1.224 psf (58.605 N/m^2) at a freestream Mach number of 1.5 to 0.671 psf (32.127 N/m^2), while maintaining constant lift. For Lockheed Martin's point of departure aircraft, a tenfold reduction of the initial shock pressure rise on the ground is demonstrated, from 1.623 psf (77.71 N/m^2) at a freestream Mach number of 1.5 to 0.152 psf (7.278 N/m^2), also while maintaining constant lift.

I. Introduction

THE topic of sonic boom flourished in the 1960s with the advent of the Supersonic Transport project which was canceled in 1971, then in the mid-1980s to mid-1990s with the subsequent High Speed Civil Transport (HSCT) program, and was recently resurrected by the Defense Advanced Research Projects Agency (DARPA) Quiet Supersonic Platform (QSP) project. Whereas the practical specifications for the Boeing HSCT called for a 292-seat supersonic aircraft with a gross takeoff weight of 900,000 lbs and assumed subsonic overland flight until further validation of the low-boom design process [1], DARPA's recent QSP project[¶] focused on phase I on a smaller aircraft with a gross takeoff weight of 100,000 lbs, but with improved capabilities that include flight over land without adverse sonic boom consequences. For this reason, the QSP project called for a design procedure that minimizes, in general, the sonic boom effects and limits, in particular, the initial shock pressure rise (ISPR) on the ground to less than 0.3 psf (14.364 N/m^2).

Sonic boom minimization began with Busemann who explained in 1935 how to eliminate the wave drag and sonic boom due to an aircraft's volume, then noted in 1955 that the lift contribution to both issues is inescapable. The first minimum for a full signature was given in the form of a lower bound by Petty [2] who determined the minimum shock strength under the provision that the absolute value of the overpressure be everywhere less than or equal to the front shock pressure rise. Today, most if not all practitioners of sonic boom prediction and minimization rely on the F function introduced by Whitham [3] as part of the modified linear theory (MLT) he developed to analyze the supersonic wave field of an axisymmetric projectile. This special function provides a relatively simple and direct relationship between the cross-sectional area of a slender, axisymmetric body and the near-field pressure distribution. The MLT "corrects" the original linearized theory with second-order effects to track the propagation of near-field waves into the bow and tail shock of the "N-wave" asymptotic far-field solution. Lomax [4] and Walkden [5] established the basis for applying Whitham's theory for axisymmetric bodies to nonaxisymmetric lifting bodies, where the lift contributes an additional component to the cross-sectional area of an "equivalent body of revolution." These developments provide for a three-dimensional F function, one that might be different in each azimuthal plane that passes through the freestream axis of each equivalent body. In each azimuthal plane of the cylindrical wave field, the F function and the corresponding pressure signature would appear to be generated by a different equivalent body of revolution.

The Jones–Seebass–George–Darden (JGSD) sonic boom minimization theory [6] named for the primary contributors to its development, culminated the F-function approach for sonic boom theory—a theory that arguably remains state of the art. For a given aircraft length, weight, Mach number, and altitude, the JGSD theory prescribes the cross-sectional area distribution of a slender aircraft that separately minimizes one of three sonic boom minimization parameters: total impulse, ISPR, and the ISPR followed in a finite rise time by a maximum pressure (Fig. 1). These optimal area distributions are determined by prescribing a special F function that evolves into the asymptotic pressure signature with one of the selected sonic boom parameters minimized. The minimized signatures include the effects from propagation through an isothermal

*Professor, Department of Mechanical Engineering and Institute for Computational and Mathematical Engineering, Mail Code 3035. Fellow AIAA.
†Associate Professor, Department of Aerospace Engineering Sciences, Campus Box 429. Member AIAA.
‡Associate Professor, Department of Aerospace Engineering Sciences, Campus Box 429, Associate Fellow AIAA.
§Assistant Professor, Faculty of Aeronautics and Astronautics, Department of Astronautical Engineering, Division of Aerospace Environment and Systems, Ayazaga Campus. Member AIAA.
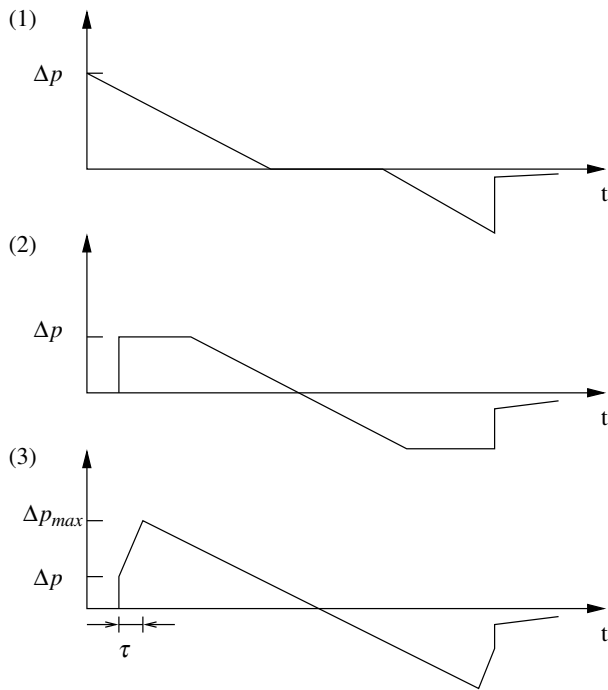
Fig. 1   Overpressure signatures: (1) minimum impulse with an ISPR of Δp; (2) minimum ISPR Δp; (3) minimum overpressure with ISPR Δp, followed in a finite rise time τ by a maximum pressure Δp_{max}.

atmosphere. With all other design parameters fixed, the theory predicts a critical vehicle equivalent length, above which a shock-free (thus boom-free) solution is realized. Unfortunately, this length far exceeds structural and material limitations of current technology.

There is a fundamental shortcoming of the JGSD theory for real aircraft design: it only provides an area distribution. Because both the physical volume and lift distribution contribute to the cross-sectional area distribution of the equivalent body, the distributions defined by the JGSD are not unique. However, the volume, lift, and stability constraints of configurations with reasonable flying qualities limit the realistic design space. Although physical constraints limit the production of far-field pressure signatures, wind tunnel tests (for example, see [7]) have verified that JGSD-designed models approach the minimized boom signature shapes.

The typical iterations used in JGSD design start with computing the lift distribution of a candidate vehicle in trimmed supersonic cruise. The cross-sectional area distribution of the equivalent body of revolution (again, usually in the plane beneath the vehicle) is then computed, accounting for both the volume and lift contributions. The F function is then computed from the equivalent body, and then compared to the appropriate JGSD F function that minimizes the selected sonic boom parameter. The next iteration cycle now starts with the designer making changes to the original configuration so that its F function approaches the JGSD ideal. This approach is typical of low-boom design processes during the 1960s and 1970s [8–10].

In his exploration of methods to reduce undesirable pressure signatures from large supersonic aircraft, McLean [11] introduced a formula to compute an approximate ground pressure signature for a given F function. This provided a rapid means of predicting changes in the ground signature from changes in a vehicle's cross-sectional area distribution and corresponding F function. Like the JGSD theory, however, McLean's formula only allows for the computation of the asymptotic N wave. Within this N-wave constraint, however, the formula does allow the designer to explore more general F functions than those specified in the JGSD theory.

Acoustic propagation codes such as the ARAP code [12] were developed to more accurately model the propagation of the aircraft acoustic signature through the real atmosphere. These codes account for the second-order effects associated with the propagation of weak shocks that accumulate to first order. A real atmosphere model, for example, the U.S. Standard Atmosphere, is incorporated along with winds. These codes directly compute the propagation of the pressure field starting from the F function or its corresponding pressure field in the MLT near field. They make no a priori assumptions for the shape of the ground signature; thus, they provide a means for examining ground signatures that might contain more than two shocks.

The two-shock ground signature of the N wave or the "shaped" signatures of JGSD severely limit the available design space for vehicles that might provide a more acceptable signature. As stated earlier, wind tunnel tests indicate that the pressure signatures of JGSD-designed models approach the predicted signature shapes. These are the ground signatures, however, that minimize the worst case—that is, a two-shock signature. These two-shock signatures are developed assuming that all intermediate shocks generated near the vehicle coalesce into the bow and tail shocks before reaching the ground. According to the JSGD theory, the lowest ISPR ground signature for an N wave occurs when intermediate shocks and compressions merge into the bow and tail shock as close to the vehicle as possible, with the result that a blunt-nosed vehicle produces a reduced ISPR [9,13] by taking advantage of the maximum shock attenuation path through the atmosphere. Of course, this ISPR reduction occurs at the expense of maximum drag. Darden [9] discusses the particulars of nose bluntness and presents a method for relaxing the blunt-nose constraint while retaining the major features of JGSD minimization.

It is clear that the ISPR is further minimized if the bow shock is created as weak as possible and with minimal coalescence of intermediate shocks. This could result in a multiple (more than two) ground signature. Hayes and coworkers [14] recognized the possibility of a "frozen" midfield signature at some altitude above the ground. Thus, a midfield signature containing multiple shocks might be frozen at a relatively high altitude and continue to attenuate before reaching the ground to produce lower shock overpressures than would be possible with two shocks. Argrow et al. [15] provide additional discussion of signature freezing.

In summary, most if not all linearized sonic boom theories and studies have posed the appropriate sonic boom minimization question in terms of the aircraft's equivalent body of revolution and attempted to solve the problem of how to shape the *equivalent body of revolution* in the vertical plane below the aircraft rather than how to shape the *true geometry* of the aircraft to minimize one of the three ground signature parameters (Fig. 1) mentioned previously [6]. For this reason, and to the best of the authors' knowledge, all current low-boom design methods are dominated by the procedure consisting of determining first the optimal equivalent body of revolution, evaluating its Whitham F function [3], and then manually iterating on an initial aircraft design to force its Whitham F function to match as closely as possible that of the optimal equivalent body of revolution. Such a design procedure, even when benefiting from existing charts such as those provided by Darden [16] for documenting what sonic boom levels could be achieved for a transport aircraft operating at Mach numbers of 2.5 and 3.2, remains cumbersome and inefficient.

Recently, Yamaguchi and Nakamura [17] improved the shape-based sonic boom minimization procedure of the 1960s and 1970s by automating its manual iterations and driving them by a genetic optimization algorithm. Although their approach is also based on the MLT [3], it operates on the true geometry of the aircraft and therefore is less cumbersome and more efficient than previously developed and practiced approaches. In this paper, an alternative, low-boom shaping methodology for supersonic aircraft is presented for mitigating the ISPR. This methodology, along with that proposed in [17], shares the concept of operating directly on the true geometry of an aircraft rather than on the equivalent body of revolution. However, it differs from the work described in [17] in at least three aspects: 1) it combines elements from both the linearized and nonlinear aero-dynamic theories, 2) it exploits the latest advances in computational fluid dynamics (CFD) for predicting the lift distribution and performing its sensitivity analysis, and 3) it relies on a gradient-based three-model oriented optimization procedure with a proven track
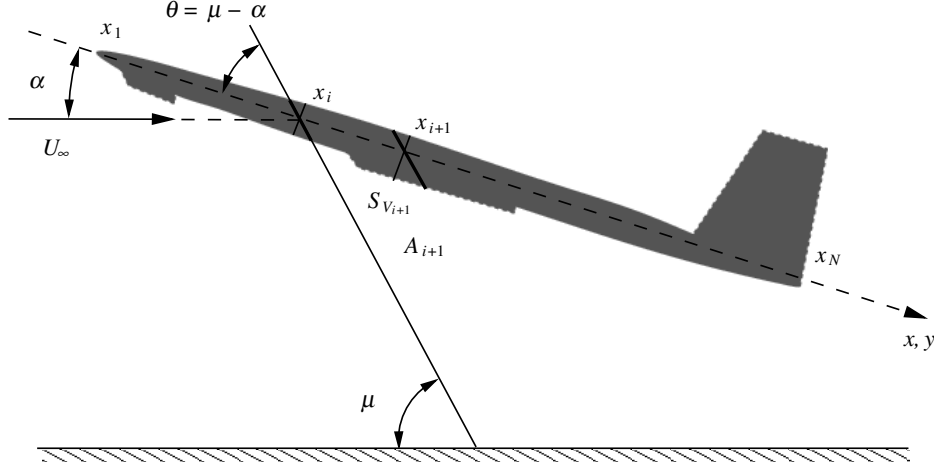
Fig. 2 x axis, Mach angle μ, angle of attack α, angle θ, and cross-sectional areas A_i and S_{V_i}.

record [18]. More important, this computational technology, which was developed by the authors under DARPA's QSP program, was exercised with the optimization of two different supersonic platforms designed by Reno Aeronautical (RA) and Lockheed Martin (LM), also under DARPA's QSP program. For RA's laminar-flow supersonic aircraft and the Mach number $M_\infty = 1.5$, it suggested the possibility of reducing by almost one-half the ISPR on the ground, from 1.224 psf (58.605 N/m^2) to 0.671 psf (32.127 N/m^2) while maintaining constant lift. For LM's point of departure (POD) aircraft, it suggested that a tenfold reduction of the ISPR on the ground, from 1.623 psf (77.71 N/m^2) to 0.152 psf (7.278 N/m^2), is also achievable while maintaining constant lift but increasing by 9% the combined induced and wave drag. The remainder of this paper describes this computational-based low-boom shaping methodology and reports on its application to the RA and LM supersonic aircraft.

II.   Formulation of a Sonic Boom Minimization Problem

Here, Whitham's linearized theory for predicting the mid- and far-field pressure signatures at supersonic speeds is adopted, because of its acceptance by the sonic boom community as well as its appealing computational simplicity. For this purpose, the abscissa along an axis whose origin is located at or near the nose of the aircraft and which runs parallel to the fuselage is denoted by x (Fig. 2), and the ' superscript is used to designate the derivative with respect to x. On the other hand, to properly capture shocks, the nonlinear aerodynamic theory is adopted for evaluating the pressure distribution in the near field.

A.   Midfield Signature

In the midfield region, that is, the region centered about Mach waves in which the distance away from the Mach waves is small compared to the distance away from the aircraft, the linearized aerodynamic theory predicts the ISPR by the following formula [3]:

$$\frac{\Delta p}{p_r} = \frac{2^{\frac{5}{4}}}{z^{\frac{3}{4}}} \frac{\gamma}{\sqrt{\gamma + 1}} \left(M_\infty^2 - 1\right)^{\frac{1}{8}} \sqrt{\int_0^{y^0} F(y)\, dy} \tag{1}$$

where Δp is the pressure rise, p_r is a reference pressure, z is the flight altitude, γ is the ratio of specific heats, M_∞ is the Mach number in the freestream, F is the Whitham F function, and y^0 is its balance point [3]

$$F(y^0) = 0 \tag{2}$$

Let μ denote the Mach angle defined by

$$\mu = \sin^{-1}\frac{1}{M_\infty} \tag{3}$$

and α denote the angle of attack. Under the assumption that the cross-sectional area $A(x)$ generated by the intersection of the aircraft and the planes forming a constant angle θ with the x axis (see Fig. 2) is a C^2 function (a function with continuous first and second derivatives), and that $A'(x)$ and $A''(x)$ have bounded variations, $F(y)$ has the following form:

$$F(y) = \frac{1}{2\pi}\int_0^y \frac{S_V''(x) + S_L''(x)}{\sqrt{y - x}}\, dx \tag{4}$$

where S_V denotes the cross-sectional area due to volume of the equivalent body of revolution and is given by

$$S_V(x) = A(x)\sin\theta \tag{5}$$

and S_L denotes the cross-sectional area due to lift of the equivalent body of revolution and is given by

$$S_L(x) = \frac{\beta}{\rho_\infty U_\infty^2}\int_0^x l(\xi)\, d\xi \tag{6}$$

In Eqs. (3) and (4), $\beta = \sqrt{M_\infty^2 - 1}$ is the Prandtl–Glauert factor, ρ_∞ and U_∞ are the freestream density and speed, respectively, and l denotes the lift distribution along the x axis.

As stated earlier, in this work the lift distribution is predicted by CFD. More specifically, the supersonic flow is modeled by the Euler equations and these nonlinear equations are solved as described in Sec. III.D to obtain the pressure distribution on the surface of the aircraft.

Furthermore, to account for multiple shocks in the midfield, the balance point y^0 is computed as the root y_j of F in $[0, L]$, where L denotes the length of the aircraft, which maximizes the value of [19]

$$\int_0^{y_j} F(y)\, dy$$

B.   Ground Signature

If one assumes that multiple shocks present in the near or midfield coalesce before reaching the ground, one can determine the sonic boom ground ISPR from Eq. (1) after defining an appropriate reference pressure p_r which accounts for the variation of atmospheric pressure and temperature between the flight altitude and the ground. For shape optimization, and only for this purpose, this assumption, which is justified in Sec. II.C, is made, p_r is defined as the geometric mean of the pressure at the flight altitude p_a and the pressure on the ground p_g [19]

$$p_r = \sqrt{p_a p_g} \tag{7}$$

and the ISPR on the ground is therefore estimated by

$$\Delta p = \frac{2^{\frac{5}{4}}}{z^{\frac{3}{4}}} \frac{\gamma}{\sqrt{\gamma+1}} \left(M_\infty^2 - 1\right)^{\frac{1}{8}} \sqrt{p_a p_g \int_0^{y^0} F(y)\,dy} \qquad (8)$$

C. Constrained Functional Minimization

When multiple shocks present at flight altitude coalesce into a bow shock and a tail shock before reaching the ground, the pressure signature they generate on the ground is an N wave with an ISPR higher than when these shocks do not coalesce but rather generate a multiple-shock ground signature. Hence, predicting the ISPR, for the purpose of shape optimization, by Eq. (8) which assumes an N-wave ground signature is justified by the fact that assuming a two-shock system on the ground is equivalent to assuming the worst case scenario for sonic boom.

From Eq. (8), it follows that the shape optimization problem for minimizing the ISPR can be formulated as follows:

Find an aircraft shape Γ which minimizes

$$G(\Gamma) = \int_0^{y^0(\Gamma, S_V(\Gamma), S_L(\Gamma))} F(S_V(\Gamma), S_L(\Gamma), y)\,dy \qquad (9)$$

under a set of N_C constraints

$$C_i(\Gamma) \geq 0 \qquad i = 1, \dots, N_C \qquad (10)$$

Equation (9) recognizes the dependency of F on Γ via the dependency of S_V and S_L on Γ [see Eq. (4)], and the dependency of y^0 on Γ via its dependency on the length of the aircraft and on F [see Eq. (2)]. Typical constraints are performance constraints such as the lift, drag, and lift-to-drag ratio.

However, *after optimization*, the ARAP propagation code [12,20] is used rather than Eq. (8) to evaluate the ISPR of the final aircraft configuration, because this code is capable of predicting correctly the desirable multiple-shock ground signatures.

D. Shape Parameterization

Because the design of a supersonic aircraft must address many issues besides sonic boom, the objective of an aircraft shaping technology for sonic boom minimization is more often to tune or optimize an initial aerodynamic shape to minimize sonic boom effects, rather than to design from scratch such a shape. For this reason, it is assumed here that an initial shape Γ^0 of the aircraft is available. Furthermore, Γ is parameterized as follows:

$$\Gamma = \Gamma(\mathbf{p}) \qquad (11)$$

where

$$\mathbf{p} = [p_1 \cdots p_{N_p}]^T \in \mathbb{R}^{N_p} \qquad (12)$$

N_p denotes the total number of shape parameters p_j, and the superscript T designates the transpose operation. Then, the minimization problem (9) and (10) is projected onto a finite-dimensional subspace to be transformed into the parameter finding problem:

Find $\mathbf{p} \in \mathbb{R}^{N_p}$ which minimizes

$$G(\mathbf{p}) = \int_0^{y^0(\mathbf{p}, S_V(\mathbf{p}), S_L(\mathbf{p}))} F(S_V(\mathbf{p}), S_L(\mathbf{p}), y)\,dy \qquad (13)$$

under a set of N_C constraints

$$C_i(\mathbf{p}) \geq 0 \qquad i = 1, \dots, N_C \qquad (14)$$

III. Computational Framework

Next, the minimization problem (13) and (14) is further discretized to enable its solution by a numerical method.

A. Discretization of the F Function

The Whitham F function is approximated here by finite elements (FE). For this purpose, the portion of the x axis along which the cross-sectional area $A(x)$ and lift distribution $l(x)$ are defined is discretized by N points of coordinates $x_1 = 0, x_2, \dots, x_N = L$, and $N - 1$ elements $[x_i, x_{i+1}]$. Equation (4) suggests that any FE approximation of $S_V(x)$ and $S_L(x)$ should be at least C^1 continuous, and with a second derivative that does not vanish everywhere inside an element.

In view of the above remarks, $S_V(x)$ is approximated in each element $[x_i, x_{i+1}]$ as follows:

$$S_V(x) = \psi_1^i(x)S_{V_i} + \psi_2^i(x)S_{V_{i+1}} + \psi_3^i(x)S'_{V_i} + \psi_4^i(x)S'_{V_{i+1}} \qquad (15)$$

where $\{\psi_j^i\}_{j=1}^{j=4}$ are the standard cubic Hermitian polynomials defined on the ith element $[x_i, x_{i+1}]$, $S_{V_i} = S_V(x_i)$, and $S'_{V_i} = S'_V(x_i)$. At the end of each kth iteration of the shape optimization procedure and after the iterate shape

$$\Gamma^k = \Gamma(\mathbf{p}^k) \qquad (16)$$

is reconstructed, S_{V_i} and S'_{V_i} are reevaluated at each point x_i using the *automatic slicer* overviewed in Sec. III.C.

To avoid a spurious finite element locking type of phenomenon, the contribution to $S_L(x)$ of each finite element is approximated by a cubic polynomial. From Eq. (6), it follows that 1) it suffices for this purpose to approximate $l(x)$ in each element by a quadratic polynomial, and 2) the FE approximation of $l(x)$ need not be C^1 continuous across the element boundaries. To this effect, N is chosen among odd integers,

$$N = 2M + 1 \qquad (17)$$

3-noded elements $x_{2m-1}{:}x_{2m}{:}x_{2m+1}$ are considered, and $l(x)$ is approximated in each element $[x_{2m-1}, x_{2m+1}]$ as follows:

$$l(x) = \phi_1^m(x)l_{2m-1} + \phi_2^m(x)l_{2m+1} + \phi_3^m(x)l_{2m} \qquad (18)$$

where $\{\phi_j^m\}_{j=1}^{j=3}$ are the standard one-dimensional finite element quadratic polynomials defined on each mth 3-noded element $[x_{2m-1}, x_{2m-1}]$, and $l_{2m-1} = l(x_{2m-1})$, $m = 1, \dots, M$. This results in the following FE approximation of $S_L(x)$ for

$$x_1 \leq x_{2m-1} \leq x < x_{2m+1}, \quad \forall\, 1 \leq m < M$$

$$S_L(x) = \bar{\Phi}_m + \Phi_1^m(x)l_{2m-1} + \Phi_2^m(x)l_{2m+1} + \Phi_3^m(\xi)l_{2m} \qquad (19)$$

where

$$\bar{\Phi}_m = \sum_{n=1}^{m-1} \left(\bar{\Phi}_1^n l_{2n-1} + \bar{\Phi}_2^n l_{2n+1} + \bar{\Phi}_3^n l_{2n} \right) \qquad (20)$$

$$\bar{\Phi}_j^n = \frac{\beta}{\rho_\infty U_\infty^2} \int_{x_{2n-1}}^{x_{2n+1}} \phi_j^n(\xi)\,d\xi, \qquad j = 1, 2, 3 \qquad (21)$$

and

$$\Phi_j^m(x) = \frac{\beta}{\rho_\infty U_\infty^2} \int_{x_{2m-1}}^{x} \phi_j^m(\xi)\,d\xi, \qquad j = 1, 2, 3 \qquad (22)$$
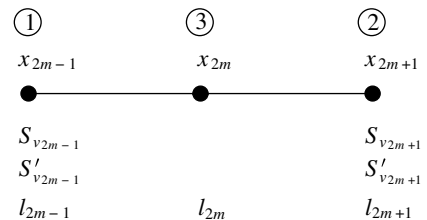

Fig. 3 The SB finite element: cubic Hermitian polynomials for $S_V(x)$ using the nodes locally labeled 1 and 2, and quadratic polynomials for $l(x)$ using the nodes 1 and 2 as well as the midside node locally labeled 3.

Again, at the end of each kth iteration of the shape optimization procedure and after Γ^k is reconstructed, l_i is reevaluated at each point x_i using the automatic slicer overviewed in Sec. III.C.

For practical purposes, both discretizations of $S_V(x)$ and $S_L(x)$ are combined into the single sonic boom (SB) finite element that is graphically depicted in Fig. 3. Furthermore, the reader is reminded that the discrete quantities S_{V_i}, S'_{V_i}, and l_i depend on the shape parameters p_j. Therefore, Eqs. (15) and (19) are rewritten as follows for

$$x \in [x_{2m-1}, x_{2m+1}]$$

$$S_V(x) = \psi_1^m(x) S_{V_{2m-1}}(\mathbf{p}) + \psi_2^m(x) S_{V_{2m+1}}(\mathbf{p}) + \psi_3^m(x) S'_{V_{2m-1}}(\mathbf{p})$$
$$+ \psi_4^m(x) S'_{V_{2m+1}}(\mathbf{p})$$

$$S_L(x) = \bar{\Phi}_m + \Phi_1^m(x) l_{2m-1}(\mathbf{p}) + \Phi_2^m(x) l_{2m+1}(\mathbf{p})$$
$$+ \Phi_3^m(x) l_{2m}(\mathbf{p})$$

(23)

Let

$$\kappa = \frac{\beta}{\rho_\infty U_\infty^2}$$

(24)

From Eqs. (4), (23), and (24) and the properties of FE shape functions, it follows that the FE discretization of the Whitham F function outlined above can be expressed as follows:

$$F(\mathbf{S}_V(\mathbf{p}), \mathbf{S}_L(\mathbf{p}), y) = \frac{1}{2\pi} \sum_{m=1}^{M} \Big(c_1^m(y) S_{V_{2m-1}}(\mathbf{p}) + c_2^m(y) S_{V_{2m+1}}(\mathbf{p})$$
$$+ c_3^m(y) S'_{V_{2m-1}}(\mathbf{p}) + c_4^m(y) S'_{V_{2m+1}}(\mathbf{p}) + d_1^m(y) l_{2m-1}(\mathbf{p})$$
$$+ d_2^m(y) l_{2m+1}(\mathbf{p}) + d_3^m(y) l_{2m}(\mathbf{p}) \Big)$$

(25)

where $\mathbf{S}_V$ and $\mathbf{S}_L$ denote the vectors of discrete values of S_V and S_L, respectively,

$$c_j^m(y) = \begin{cases} \int_{x_{2m-1}}^{x_{2m+1}} \frac{\psi_j''^m}{\sqrt{y-x}} \, dx, & x_{2m+1} \le y \\ \int_{x_{2m-1}}^{y} \frac{\psi_j''^m}{\sqrt{y-x}} \, dx, & x_{2m-1} < y < x_{2m+1} \\ 0, & y \le x_{2m-1}, \end{cases}$$

(26)

$$d_j^m(y) = \begin{cases} \kappa \int_{x_{2m-1}}^{x_{2m+1}} \frac{\phi_j''^m}{\sqrt{y-x}} \, dx, & x_{2m+1} \le y \\ \kappa \int_{x_{2m-1}}^{y} \frac{\phi_j''^m}{\sqrt{y-x}} \, dx, & x_{2m-1} < y < x_{2m+1} \\ 0, & y \le x_{2m-1} \end{cases}$$

and $\sum$ denotes the usual FE assembly process. Given the choice made for the shape functions, $c_j^m(y)$ and $d_j^m(y)$ can be evaluated analytically.

B. Discretization of the Shape Minimization Problem

Substituting Eq. (25) into Eq. (13) and discretizing the inequalities (14) generates the following discrete shape optimization problem:
Find $\mathbf{p} \in \mathbb{R}^{N_p}$ which minimizes

$$G(\mathbf{p}) = \frac{1}{2\pi} \sum_{m=1}^{M} \Big(e_1^m(y^0) S_{V_{2m-1}}(\mathbf{p}) + e_2^m(y^0) S_{V_{2m+1}}(\mathbf{p})$$
$$+ e_3^m(y^0) S'_{V_{2m-1}}(\mathbf{p}) + e_4^m(y^0) S'_{V_{2m+1}}(\mathbf{p}) + f_1^m(y^0) l_{2m-1}(\mathbf{p})$$
$$+ f_2^m(y^0) l_{2m+1}(\mathbf{p}) + f_3^m(y^0) l_{2m}(\mathbf{p}) \Big)$$

(27)

under the constraints

$$\mathbf{C}(\mathbf{p}) \ge 0$$

(28)

where

$$e_j^m(y^0) = \begin{cases} \int_0^{y^0} c_j^m(y) \, dy, & y^0 > x_{2m-1} \\ 0, & y^0 \le x_{2m-1} \end{cases}$$

$$f_j^m(y^0) = \begin{cases} \int_0^{y^0} d_j^m(y) \, dy, & y^0 > x_{2m-1} \\ 0, & y^0 \le x_{2m-1} \end{cases}$$

(29)

and $\mathbf{C}$ is the N_C-long vector of discrete constraints. Again, for the choice of shape functions ψ_j and ϕ_j made here, $e_j^m(y^0)$ and $f_j^m(y^0)$ can be computed analytically.

C. Automatic Slicing

Given a freestream Mach number M_∞ and an angle of attack α, evaluating the cross-sectional area of the equivalent body of revolution at a point x_i requires solving a computational geometry problem. For this purpose, an automatic slicer, AS, was developed. This slicer operates on an unstructured surface mesh of the target aircraft. Essentially, AS extracts the faces of this surface mesh, then constructs the slices corresponding to the intersection of these faces with the planes forming a constant angle $\theta = \mu - \alpha$ with the x axis (fuselage) and passing through the points x_i, $i = 1, \ldots, 2M + 1$ (Fig. 2). These slices are stored in a data structure suitable not only for evaluating the cross-sectional areas $A_i = A(x_i)$ and $S_{V_i} = A_i \sin \theta$ at the odd-numbered points, but also for interpolating the pressure values at all intersection points from the computed pressure values at the surface grid points, then integrating numerically the pressure field along all slice outlines to compute the values $l_i = l(x_i)$ of the lift distribution at all $2M + 1$ points.

More specifically, if the x axis is discretized by $2M + 1$ "principal" points, AS generates $4M + 1$ aircraft slices corresponding to these principal points as well as to another set of $2M$ points that bracket the odd-numbered principal points. These "bracketing" points are defined by

$$x_{2m-1^+} = x_{2m-1} + \epsilon, \qquad m = 1, \ldots, M$$
$$x_{2m-1^-} = x_{2m-1} - \epsilon, \qquad m = 2, \ldots, M + 1$$

(30)

where ϵ is a specified small quantity. AS computes the cross-sectional area S_V of the equivalent body of revolution at the odd-numbered principal points and their bracketing points, then estimates the values of S'_V at the odd-numbered principal points by finite differences as follows:

$$S'_{V_1} = \frac{S_{V_{1^+}} - S_{V_1}}{\epsilon} \qquad S'_{V_{2m-1}} = \frac{S_{V_{2m-1^+}} - S_{V_{2m-1^-}}}{2\epsilon}$$
$$m = 2, \ldots, M \qquad S'_{V_{2M+1}} = \frac{S_{V_{2M+1}} - S_{V_{2M+1^-}}}{\epsilon}$$

(31)

D. CFD-Based Prediction of the Lift Distribution

As stated earlier, in this work the pressure distribution in the near field is computed by means of CFD. More specifically, the AERO-F [21] flow code developed at the University of Colorado for the solution of nonlinear aeroelastic problems is adopted. This code can model a flow either by the Euler equations, or by the Reynolds averaged Navier–Stokes equations, or by a large eddy simulation. AERO-F combines a Galerkin centered approximation for the viscous terms, and a Roe upwind scheme for the convective fluxes. It achieves higher-order spatial accuracy through the use of a multidimensional piecewise linear reconstruction that follows the principle of the monotonic upwind scheme for conservative laws [22]. AERO-F performs time and pseudotime integration on fixed as well as moving grids by a geometrically conservative extension of the second-order implicit three-point backward difference scheme. It solves all linearized systems of equations in parallel by the restricted additive Schwarz (RAS) preconditioned GMRES iterative algorithm [23].

AERO-F is designed to operate also on moving grids. These are relevant to CFD-based shape optimization because shape modifications incur surface grid modifications which in turn entail

volume grid modifications. Generating a new CFD mesh for each intermediate shape, Γ^k can be cumbersome and CPU-wise prohibitive. Alternatively, the initial CFD grid can be deformed at each iteration k to conform to the evolving shape Γ^k, as typically done in nonlinear time-dependent aeroelastic computations. AERO-F enables such a computational strategy by offering several robust methods for constructing dynamic meshes. Among these stands out the torsional springs method [24,25] which constructs a fictitious stiffness for each fluid mesh element that increases to infinity when the volume of that element decreases to zero. This prevents all collapsing mechanisms (node to node, node to edge, and node to face) from occurring when updating the CFD dynamic mesh at each iteration of the optimization procedure.

E. Computation of the Balance Point

For a given Γ^k, the corresponding balance point y^{0^k} is computed by applying the bisection algorithm to the discretized F function (25) to extract its roots $0 < y_j^k < L^k$, and choosing that root which maximizes

$$\int_0^{y_j^k} F(\mathbf{S}_V(\mathbf{p}^k), \mathbf{S}_L(\mathbf{p}^k), y) \, \mathrm{d}y$$

IV. Gradient-Based Optimization Methodology

Next, the solution of the minimization problem (27) and (28) by a computational strategy which combines three different numerical models, namely, the optimization, analysis, and design models [26], is described.

A. Optimization Model

In this model, the computational strategy for solving the optimization problem (27) and (28) is selected. Because for a given shape Γ^k the lift distribution is evaluated by a CFD computation, the CPU cost of the function evaluation $G(\mathbf{p}^k)$ Eq. (27) can be reasonably expected to dominate the total computational cost of the optimization process. It is well known that in such a circumstance, a gradient-based solution methodology is more appropriate than a gradient-free approach such as a genetic algorithm.

More specifically, it is chosen to solve the minimization problem (27) and (28) by a Lagrange multiplier method—that is, to transform this problem into finding the saddle point of the Lagrangian

$$\mathcal{L}(\mathbf{p}, \boldsymbol{\lambda}) = G(\mathbf{p}) + \boldsymbol{\lambda}^T \mathbf{C}(\mathbf{p}) \tag{32}$$

where $\boldsymbol{\lambda}$ is a vector of Lagrange multipliers. The Kuhn–Tucker equations associated with the above Lagrangian are derived and solved by the sequential quadratic programming (SQP) method [27]. In this method, these equations are linearized at each iteration to formulate an equivalent quadratic problem. The quadratic operator, which is the Hessian of the Lagrangian, is approximated by a rank-1 update scheme that guarantees positive definiteness. In general, the SQP method exhibits good convergence rates and requires only a few evaluations of the objective function and constraints.

B. Analysis Model

In this model, the algorithms for evaluating the optimization criteria (27) and (28) are specified. These include the automatic slicing algorithm described in Sec. III.C for evaluating the cross-sectional areas due to volume S_{V_i} of the equivalent body of revolution, and the AERO-F module overviewed in Sec. III.D for solving the Euler equations and computing the values l_i of the lift distribution. The latter equations are written in compact form as follows:

$$\mathcal{E}(\mathbf{w}(\mathbf{p}), \mathbf{x}(\mathbf{p})) = 0 \tag{33}$$

where $\mathbf{w}$ denotes the fluid state vector and depends on the shape parameters p_j, and $\mathbf{x}$ (not to be confused with the x axis or x_i points)

denotes the fluid grid position vector and is governed by the shape parameters p_j.

The following analytical sensitivity analysis of the discretized governing equations is also assigned to this model, which provides the optimization model with more robust gradients than finite differencing.

From Eq. (27), it follows that the derivative of the objective function G with respect to a shape parameter p_j is given by

$$
\begin{aligned}
\frac{\mathrm{d}G}{\mathrm{d}p_j} = \frac{1}{2\pi} \sum_{m=1}^M \Bigg(& \frac{\mathrm{d}e_1^m}{\mathrm{d}p_j} S_{V_{2m-1}} + e_1^m \frac{\mathrm{d}S_{V_{2m-1}}}{\mathrm{d}p_j} + \frac{\mathrm{d}e_2^m}{\mathrm{d}p_j} S_{V_{2m+1}} \\
& + e_2^m \frac{\mathrm{d}S_{V_{2m+1}}}{\mathrm{d}p_j} + \frac{\mathrm{d}e_3^m}{\mathrm{d}p_j} S'_{V_{2m-1}} + e_3^m \frac{\mathrm{d}S'_{V_{2m-1}}}{\mathrm{d}p_j} + \frac{\mathrm{d}e_4^m}{\mathrm{d}p_j} S'_{V_{2m+1}} \\
& + e_4^m \frac{\mathrm{d}S'_{V_{2m+1}}}{\mathrm{d}p_j} + \frac{\mathrm{d}f_1^m}{\mathrm{d}p_j} l_{2m-1} + f_1^m \frac{\mathrm{d}l_{2m-1}}{\mathrm{d}p_j} + \frac{\mathrm{d}f_2^m}{\mathrm{d}p_j} l_{2m+1} \\
& + f_2^m \frac{\mathrm{d}l_{2m+1}}{\mathrm{d}p_j} + \frac{\mathrm{d}f_3^m}{\mathrm{d}p_j} l_{2m} + f_3^m \frac{\mathrm{d}l_{2m}}{\mathrm{d}p_j} \Bigg)
\end{aligned}
\tag{34}
$$

In the above expression, each term of the form $\mathrm{d}e_i^m/\mathrm{d}p_j$ or $\mathrm{d}f_i^m/\mathrm{d}p_j$ can be computed as follows:

$$\frac{\mathrm{d}e_i^m}{\mathrm{d}p_j} = \frac{\mathrm{d}e_i^m}{\mathrm{d}y^0} \frac{\mathrm{d}y^0}{\mathrm{d}p_j} \tag{35}$$

The derivatives $\mathrm{d}e_i^m/\mathrm{d}y^0$ and $\mathrm{d}f_i^m/\mathrm{d}y^0$ are computed analytically by differentiating Eqs. (29). As for evaluating $\mathrm{d}y^0/\mathrm{d}p_j$, it is recalled that $F(\mathbf{S}_V(\mathbf{p}), \mathbf{S}_L S(\mathbf{p}), y^0) = 0$ and Eq. (25) is differentiated at the point y^0. This gives

$$
\begin{aligned}
\frac{\mathrm{d}y^0}{\mathrm{d}p_j} = \sum_{m=1}^M \Bigg(& -\frac{c_1^m(y^0)\frac{\mathrm{d}S_{V_{2m-1}}}{\mathrm{d}p_j} + c_2^m(y^0)\frac{\mathrm{d}S_{V_{2m+1}}}{\mathrm{d}p_j}}{D} \\
& -\frac{c_3^m(y^0)\frac{\mathrm{d}S'_{V_{2m-1}}}{\mathrm{d}p_j} + c_4^m(y^0)\frac{\mathrm{d}S'_{V_{2m+1}}}{\mathrm{d}p_j}}{D} \\
& -\frac{d_1^m(y^0)\frac{\mathrm{d}l_{2m-1}}{\mathrm{d}p_j} + d_2^m(y^0)\frac{\mathrm{d}l_{2m+1}}{\mathrm{d}p_j}}{D} - \frac{d_3^m(y^0)\frac{\mathrm{d}l_{2m}}{\mathrm{d}p_j}}{D} \Bigg)
\end{aligned}
\tag{36}
$$

where

$$
\begin{aligned}
D = \sum_{m=1}^M \Bigg(& \frac{\mathrm{d}c_1^m}{\mathrm{d}y^0} S_{V_{2m-1}} + \frac{\mathrm{d}c_2^m}{\mathrm{d}y^0} S_{V_{2m+1}} + \frac{\mathrm{d}c_3^m}{\mathrm{d}y^0} S'_{V_{2m-1}} + \frac{\mathrm{d}c_4^m}{\mathrm{d}y^0} S'_{V_{2m+1}} \\
& + \frac{\mathrm{d}d_1^m}{\mathrm{d}y^0} l_{2m-1} + \frac{\mathrm{d}d_2^m}{\mathrm{d}y^0} l_{2m+1} + \frac{\mathrm{d}d_3^m}{\mathrm{d}y^0} l_{2m} \Bigg)
\end{aligned}
\tag{37}
$$

All terms of the form $\mathrm{d}c_j^m/\mathrm{d}y^0$ and $\mathrm{d}d_j^m/\mathrm{d}y^0$ are computed by differentiating Eqs. (26), and relying on the automatic slicer AS described in Sec. III.C for providing analytical expressions for all quantities of the form $\mathrm{d}S_{V_{2m-1}}/\mathrm{d}p_j$ and $\mathrm{d}S'_{V_{2m-1}}/\mathrm{d}p_j$. To evaluate the derivatives of the form $\mathrm{d}l_{2m+1}/\mathrm{d}p_j$, it is noted that

$$\frac{\mathrm{d}l_{2m+1}}{\mathrm{d}p_j} = \frac{\mathrm{d}l_{2m+1}}{\mathrm{d}\mathbf{w}} \frac{\mathrm{d}\mathbf{w}}{\mathrm{d}p_j} \tag{38}$$

and $\mathrm{d}\mathbf{w}/\mathrm{d}p_j$ is computed by differentiating the governing fluid equation (33), which yields

$$\frac{\mathrm{d}\mathcal{E}}{\mathrm{d}\mathbf{w}} \frac{\mathrm{d}\mathbf{w}}{\mathrm{d}p_j} = -\frac{\mathrm{d}\mathcal{E}}{\mathrm{d}\mathbf{x}} \frac{\mathrm{d}\mathbf{x}}{\mathrm{d}p_j} \tag{39}$$

The vector $\mathrm{d}\mathbf{x}/\mathrm{d}p_j$ is computed in the design model which is overviewed in the next section. AERO-F constructs the sparse matrices $\mathrm{d}\mathcal{E}/\mathrm{d}\mathbf{w}$ and $\mathrm{d}\mathcal{E}/\mathrm{d}\mathbf{x}$ using the analytical derivations described in [18,28], respectively, and solves the above system of

equation by the RAS preconditioned GMRES iterative algorithm [23].

The derivatives of the constraint inequalities with respect to the shape parameters are computed using a similar sensitivity analysis.

C. Design Model

The design model provides an interface between the optimization and analysis models described previously. Its main purpose is to define a relationship between the position of the fluid grid points and the shape optimization parameters

$$\mathbf{x} = \mathbf{x}(\mathbf{p}) \tag{40}$$

In this work, the surface geometry g of the aircraft is described by a CFD surface mesh constructed from CAD data. The variations (or motions) Δg^k induced at each kth iteration of the optimization procedure by variations (or motions) Δp_j^k of the shape parameters p_j are approximated by Coons patches. This can be written as

$$\Delta g^k = \sum_q N_q(\eta, \zeta) \Delta p_q^k \tag{41}$$

where N_q is the qth shape function of the Coons patch, η and ζ denote the local coordinate system, and

$$\Delta p_q^k = p_q^k - p_q^{k-1} \tag{42}$$

Hence, after Δp_q^k is determined from one iteration on the optimization model, Δg^k is deduced from Eq. (41), and AERO-F's torsional spring analogy method is used to move the fluid grid position to conform to the updated surface geometry. In matrix format, this can be written as follows:

$$\begin{bmatrix} \mathbf{K}_{ii} & \mathbf{K}_{ib} \\ \mathbf{K}_{ib}^T & \mathbf{K}_{bb} \end{bmatrix} \begin{bmatrix} \Delta \mathbf{x}_i^k \\ \Delta \mathbf{g}^k \end{bmatrix} = \begin{bmatrix} \mathbf{0} \\ \mathbf{R}_b^k \end{bmatrix} \tag{43}$$

where $\mathbf{K}$ is the fictitious stiffness matrix associated with the fluid grid and constructed to prevent crossovers during the update of its position $\mathbf{x}^k$, the subscript i designates those fluid grid points lying inside the fluid computational domain, and the subscript b those lying on the aircraft surface Γ, and $\mathbf{R}_b$ is the fictitious force needed for enforcing on Γ

$$\Delta \mathbf{x}_b^k = \Delta \mathbf{g}^k \tag{44}$$

$\mathbf{R}_b$ needs not be computed as the first row of the matrix Eq. (43) can be rewritten as

$$\mathbf{K}_{ii} \Delta \mathbf{x}_i^k = -\mathbf{K}_{ib} \Delta \mathbf{g}^k \tag{45}$$

and solved to obtain the desired $\Delta \mathbf{x}_i^k$, which completes the update of the fluid grid position $\mathbf{x}^k = \mathbf{x}^{k-1} + \Delta \mathbf{x}^k$.

V. Applications

A. RA's Laminar-Flow Supersonic Aircraft

First, this section reports on the application of the low-boom shaping methodology overviewed in this paper to the optimization of the initial design of RA's QSP to lower its ISPR. The length of this
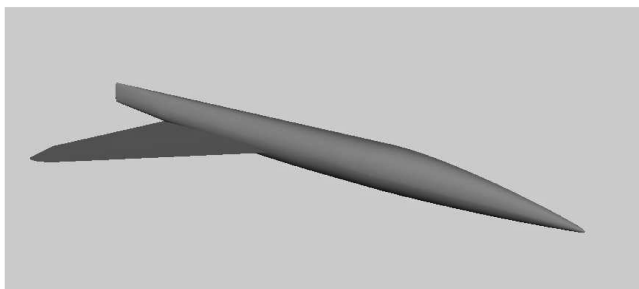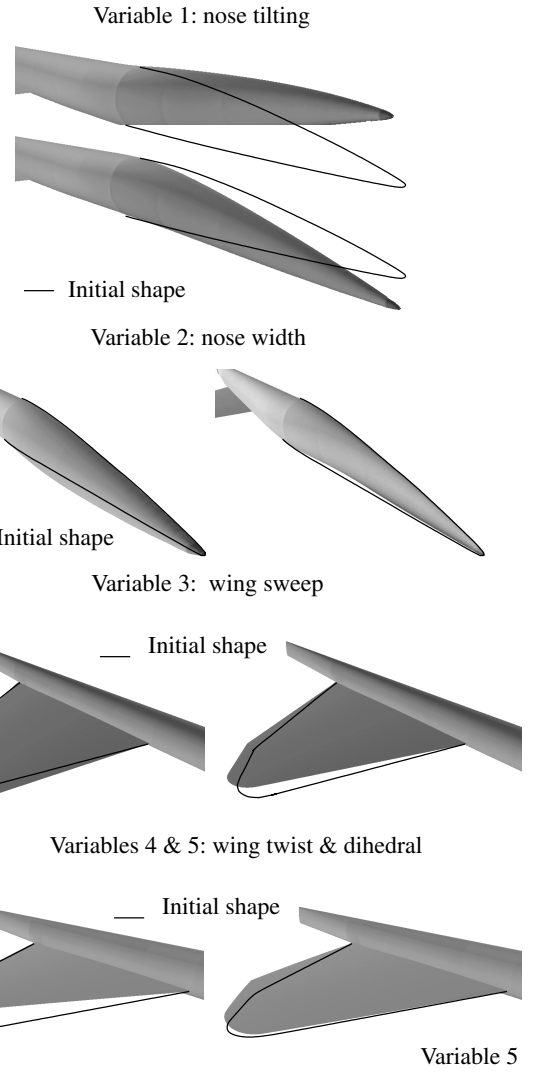

Fig. 4   Tailess half-model of RA's QSP.

Fig. 5   Shape changes for RA's QSP.

aircraft is $L = 122.22$ ft (37.253 m) and its weight is assumed here to be equal to 98,000 lbs (435,925 N). Because of symmetry, only half of the aircraft is modeled; however, all signatures are computed for the full aircraft. To reduce computational costs, the vertical tail is not modeled as it does not effectively contribute to the ISPR (this assumption was verified a posteriori). The corresponding half-model is shown in Fig. 4. It is discretized by a surface mesh with 170,356 triangles and 90,627 grid points generated using the Integrated Computer Aided Engineering and Manufacturing (ICEM) CFD software package. This software is also used to generate a volume mesh with 1,724,113 tetrahedra and 340,424 grid points.

The level-flight conditions are set to $M_\infty = 1.5$, $z = 45,000$ ft (13,716 m), and a trim angle of attack $\alpha = 1.81$ deg. For these conditions, the ISPR predicted by ARAP for the initial design characterized by the initial shape Γ^0 is equal to 1.467 psf (70.240 N/m^2); this value is about 4.9 times higher than the maximum of 0.3 psf (14.364 N/m^2) specified by DARPA for phase I of the QSP project.

Table 1   ISPR for initial and optimized shapes of RA's aircraft, predicted by Eq. (8) and by ARAP

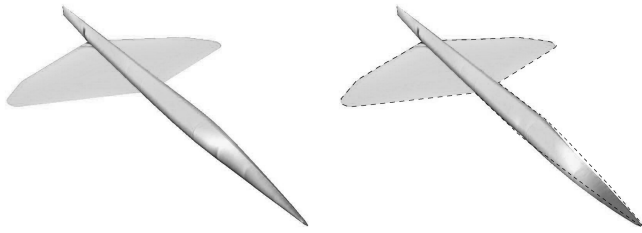|	ISPR Eq. (8)	ISPR (ARAP)
Initial shape	1.381 psf (66.123 N/m^2)	1.467 psf (70.240 N/m^2)
Optimized shape	1.224 psf (58.605 N/m^2)	0.671 psf (32.127 N/m^2)

Fig. 6 Initial and optimized shapes (with pressure contours) of RA's QSP.

Five parameters are used to optimize the initial shape using the design model approach outlined in Sec. IV.C: p_1 and p_2 control the tilting and width of the nose, and p_3, p_4, and p_5 control the sweep, twist, and dihedral of the wing. The effect of each of these parameters is illustrated in Fig. 5.

Solving the minimization problem (13) while maintaining constant lift produces the quantitative results summarized in Table 1. Equation (8), whose validity is limited to a two-shock signature, predicts a minor improvement of the initial design. However, ARAP, which is capable of predicting correctly a desirable multiple-shock ground signature, reveals a reduction of the ISPR by 54.2%. The initial and optimized shapes are compared in Fig. 6. Essentially, the shape optimization increased the width of the nose. The effects of this shape change on the variations with x of the F function are reported in Fig. 7. More specifically, Fig. 7a shows that the F functions of the initial and optimized shapes differ significantly at the nose of the aircraft. Comparing Figs. 7b and 7c reveals that this difference is due mainly to volume and to an increase of the bluntness of the aircraft's nose. The ground signatures predicted by ARAP for the initial and the optimized shapes are depicted in Fig. 8. Although the initial shape leads to a two-shock ground signature, the optimized shape produces a three-shock signature and reduces the ISPR on the ground from 1.224 psf (58.605 N/m^2) at $M_\infty = 1.5$ to 0.671 psf (32.127 N/m^2) while maintaining constant lift. However, the reduced ISPR is still above DARPA's target value of 0.3 psf (14.364 N/m^2), which suggests the need for more radical changes in the aircraft's shape.

B. LM's POD Aircraft

Next, the low-boom shaping methodology is illustrated with the optimization of LM's POD supersonic platform in view of improving its sonic boom performance. This aircraft has a length $L = 128.57$ ft (39.188 m) and a weight assumed here to be equal to 98,000 lbs (435,925 N). Because of symmetry, only half of this QSP is modeled (Fig. 9). However, all signatures are computed for the full aircraft. To represent the shape of this aircraft, a surface mesh is generated with 97,537 triangles and 49,306 grid points using the ICEM CFD software package. This software is also used to discretize the computational domain of the flow around the half-model by a volume mesh with 1,224,583 tetrahedra and 234,405 grid points.

The level-flight conditions associated with $M_\infty = 1.5$, $z = 45,000$ ft (13,716 m), and a trim angle of attack $\alpha = 0.7$ deg are considered. For these conditions, the ISPR predicted by ARAP for the initial design characterized by the initial shape Γ^0 is equal to 1.623 psf (77.71 N/m^2). Hence, this ISPR is 5.4 times higher than the limit of 0.3 psf (14.364 N/m^2) specified by DARPA for phase I of the QSP project.

The following incremental optimizations are performed. They are aimed not only at reducing the ISPR of LM's POD aircraft, but also at assessing the contribution and impact of some specific shape modifications on the sonic boom performance of a supersonic aircraft.

1) Nose tilting: This optimization focuses on the nose of the POD aircraft and searches for its optimal inclination and optimal curvature at the intersection with the fuselage. Two shape parameters are used for this purpose and the intersection between the fuselage and the nose is constrained to remain C^1 continuous.

2) Canard positioning: Here, the canard is moved along the fuselage in search of an optimal position. This optimization requires
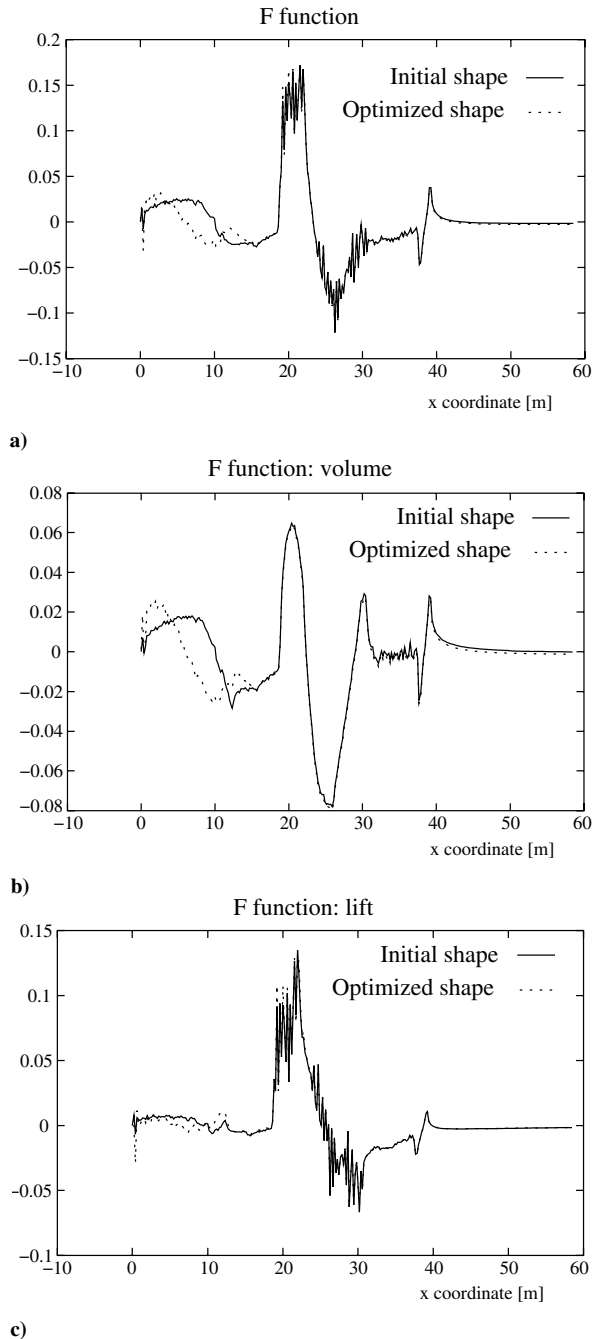

a)

b)

c)

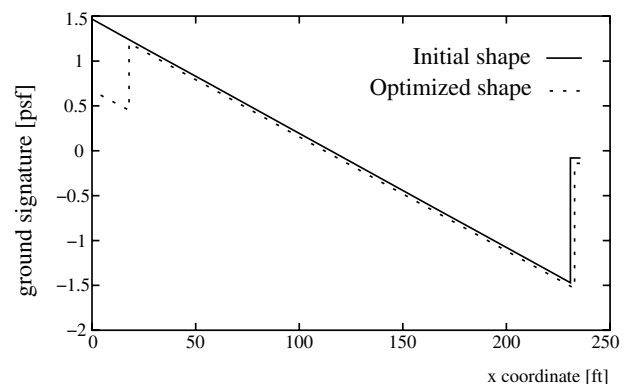**Fig. 7 Variation with x of the F function (RA's QSP).**

Fig. 8 RA's QSP [$M_\infty = 1.5$, $z = 45,000$ ft (13,716 m)]: ground signatures and initial shock pressure rises.

Fig. 9 Half-model of LM's POD aircraft.

a single parameter which is the rigid body translation of the canard along the x axis. On the other hand, this shape optimization challenges most CFD solvers not only because of the necessity of computing flows on moving grids, but most importantly because the wet and dry surfaces of the aircraft vary throughout the iterations.

3) Dihedral and sweep angles of the canard: To vary these angles, one vertical and one horizontal translational degree of freedom (dof) are introduced at each of the leading and trailing tips of the canard. Both tips are constrained to have the same motion, which results in two shape optimization parameters only.

4) Dihedral and sweep angles of the canard and the wing: Here, the previous shape optimization is applied to the canard as well as the wing, which results in four shape optimization parameters.

5) Dihedral, sweep, and twist angles of the canard and the wing: To control the twist angles of both the canard and the wing, the vertical displacement dof at the leading and trailing tips of each of the canard and the wing are allowed to move independently, which brings the total number of shape optimization parameters to six.

6) Nose tilting, and dihedral, sweep, and twist angles of the canard and the wing: In this final optimization, the eight shape parameters corresponding to the first and fifth optimizations outlined above are considered.

In each case, constant lift (equal to the weight of the POD) is maintained. The obtained reductions of the objective function G [see Eq. (27)] and the optimized values of the ISPR as predicted by Eq. (8) and the ARAP code are reported in Table 2. The reader is reminded that Eq. (8) assumes the worst case scenario of a two-shock (N wave) ground signature. The ground signatures for the initial shape (Fig. 10a) and the shapes obtained by the fourth and sixth (Fig. 10b) optimizations outlined previously are also reported in Fig. 11. Finally, the convergence of the optimization procedure is reported in Fig. 12.

The following observations are worth noting:

1) For the flight conditions stated above, the initial design of this POD aircraft generates an N-wave signature on the ground (Fig. 11).

2) The lift produced by the canard introduces bluntness to the equivalent body of revolution, reducing the ISPR as predicted by the linearized theory. The tilting of the nose appears to have a minor effect on the sonic boom performance.

3) The exact position of the canard relative to the nose of the aircraft also appears to have a minor effect on sonic boom performance.

4) On the other hand, the dihedral, sweep, and twist angles of the canard and wing appear to have a significant effect on sonic boom performance.

5) For the first four shape optimizations, Eq. (8) and the ARAP code predict essentially the same optimized ISPR values. However, for each of the last two shape optimizations, ARAP predicts a significantly lower optimized ISPR value than Eq. (8). This is

Initial shape (with pressure contours)

a)

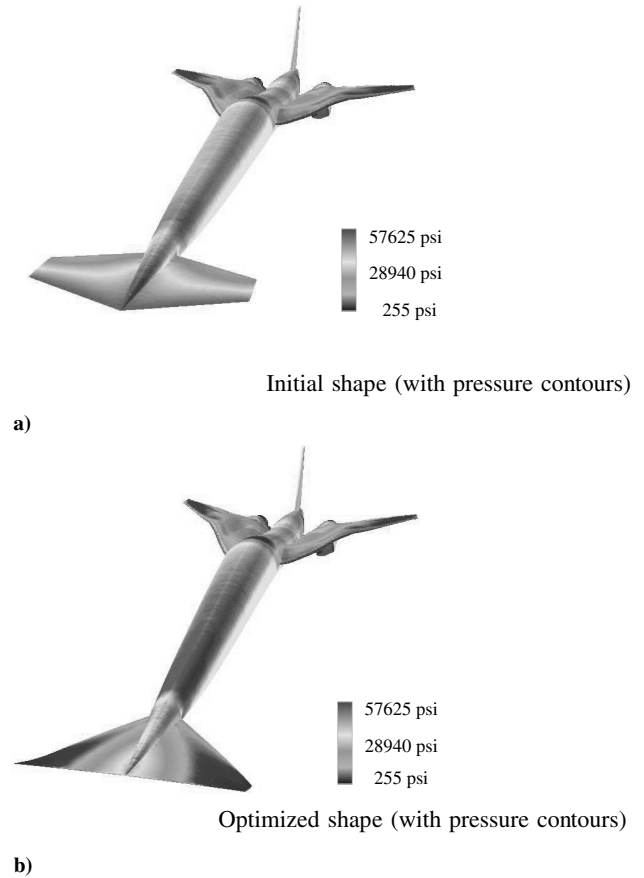Optimized shape (with pressure contours)

b)

Fig. 10 Shape optimization of LM's POD for minimum ISPR [$M_\infty = 1.5$, $z = 45,000$ ft (13,716 m)]. a): Initial shape (with pressure contours). b): Optimized shape (with pressure contours).
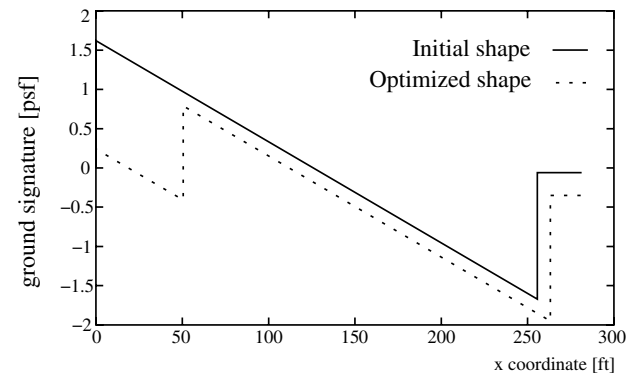

Fig. 11 LM's POD [$M_\infty = 1.5$, $z = 45,000$ ft (13,716 m)]: ground signatures and initial shock pressure rises.

because, as shown in Fig. (11) for the final shape optimization, each of the latter two optimizations produces a shape which generates on the ground a three-shock signature that cannot be captured by Eq. (8). Nevertheless, the last two shape optimizations illustrate the suitability of Eq. (8) for optimization, because in both cases the

Table 2 Incremental shape optimization of LM's POD supersonic platform

| Shape optimization	$\frac{\Delta G(\Gamma)}{G(\Gamma^0)}$	ISPR Eq. (8)	ISPR (ARAP)
Nose (tilting)	4.5%	1.551 psf (74.262 N/m²)	1.549 psf (74.166 N/m²)
Canard (positioning)	4.0%	1.558 psf (74.597 N/m²)	1.553 psf (74.358 N/m²)
Canard (dihedral and sweep)	24.9%	1.218 psf (58.318 N/m²)	1.215 psf (58.175 N/m²)
Canard and wing (dihedral and sweep)	31.5%	1.111 psf (53.195 N/m²)	1.107 psf (53.003 N/m²)
Canard and wing (dihedral, sweep, and twist)	56.0%	0.714 psf (34.186 N/m²)	0.159 psf (7.613 N/m²)
Nose (tilting) and canard and wing (dihedral, sweep, and twist)	63.4%	0.594 psf (28.441 N/m²)	0.152 psf (7.278 N/m²)
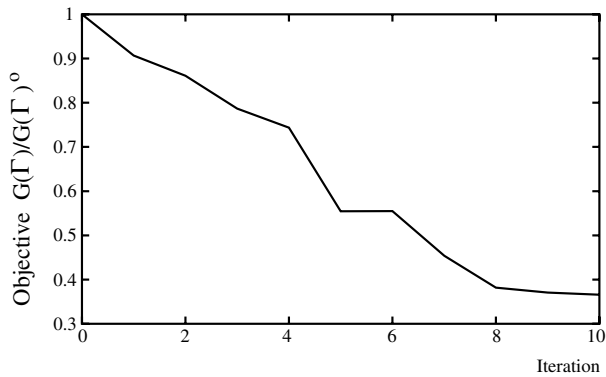
Fig. 12 LM's POD [$M_\infty = 1.5$, $z = 45,000$ ft (13,716 m)]: convergence history.

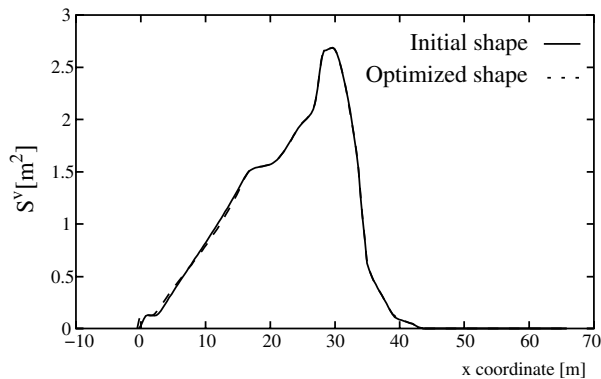**Fig. 13 Variation with x of the cross-sectional area of the equivalent body of revolution due to volume (POD aircraft).**
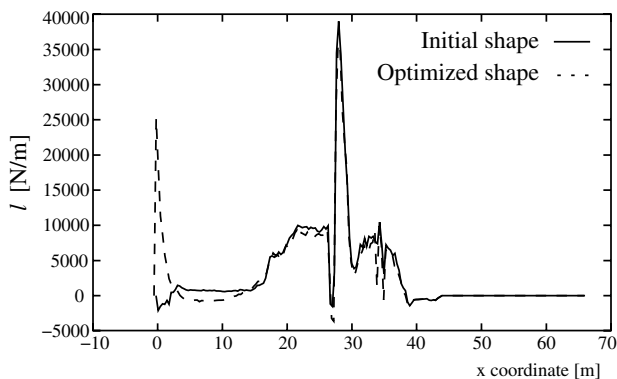

Fig. 14 Variation with x of the lift distribution l (POD aircraft).

presented computational methodology starts from a shape that generates an N-wave signature on the ground, and ends with an aerodynamic shape that generates a multishock signature on the ground.

6) For the flight conditions considered herein, and neglecting the effect of the propulsion system (no consideration of inlet spillage and exhaust flow), the final optimized shape of LM's POD aircraft (optimization no. 6) meets DARPA's goal in phase I of a minimum ISPR below 0.3 psf (14.364 N/m^2). This optimized shape is obtained in nine iterations, which highlights the efficiency of the described methodology, at least for this optimization problem.

7) However, Fig. 11 also suggests that it remains to reduce the strengths of the second and aft shocks.

The shape of the POD aircraft obtained in the final optimization (Fig. 10b) has the nose tilted down by an additional 1.8 deg, the canard surfaces swept forward by 24.9 deg with respect to the initial design, twisted positively by an additional 0.7 deg and tilted down with respect to the fuselage by another 0.3 deg, the wings swept forward by 2.2 deg with respect to the initial design, twisted

positively by an additional 0.2 deg, and tilted down with respect to the fuselage by another 3.8 deg. This shape optimization increases the combined lift-induced and wave drag at the considered flight conditions by 9%, from 14,952 lbs (66,509 N) to 16,325 lbs (72,617 N).

The effects of the above design changes on the variations with x of the cross-sectional area of the equivalent body of revolution due to volume, the lift distribution, and the F function are shown in Figs. 13–15, respectively. Figure 15a shows that the F functions of the initial and optimized shapes differ significantly at the nose of the aircraft. Figure 15b reveals that this difference is due mainly to volume, and the comparison of Figs. 13 and 15b suggests that it is more specifically due to the change in the second derivative of the cross-sectional area of the equivalent body of revolution due to volume. The variations with x of the lift distribution and lift are reported in Figs. 14 and 16, respectively, for both the initial and the optimized shapes of the POD aircraft. They reveal that the optimized
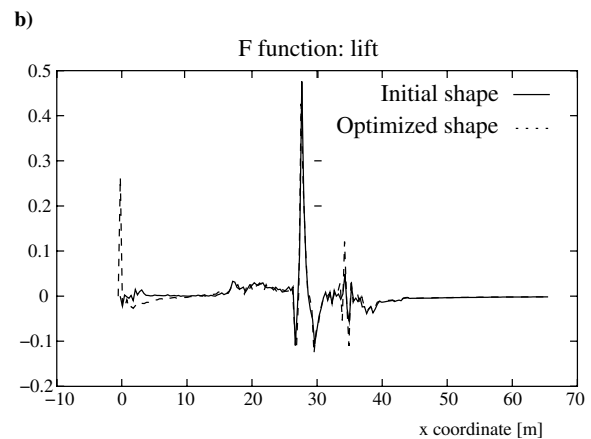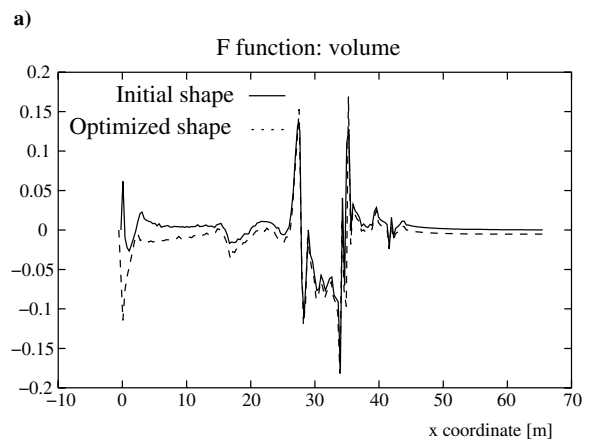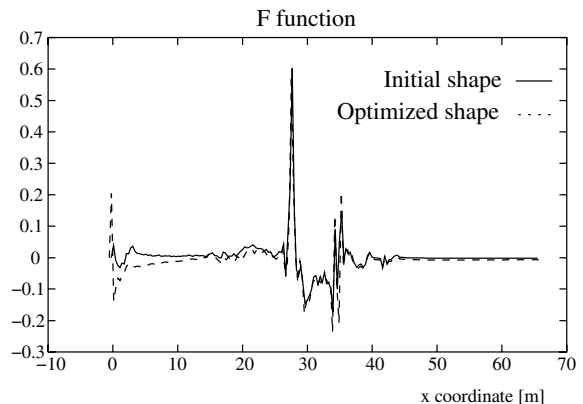

a)

b)

c)

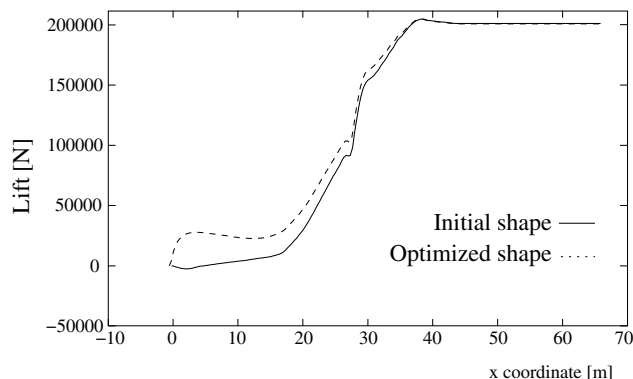**Fig. 15 Variation with x of the F function (POD aircraft).**

Fig. 16   Variation with x of the lift $\int_0^x l(\xi)\,d\xi$ (POD aircraft).

shape enjoys a greater lift, particularly at the nose of the aircraft. Hence, the design changes, and particularly those affecting the nose section and the shape of the canard increase the bluntness of the nose of the POD, thereby reducing the ISPR on the ground from 1.623 psf (77.71 N/m^2) at $M_\infty = 1.5$ to 0.152 psf (7.278 N/m^2), while maintaining constant lift but increasing by 9% the combined induced and wave drag.

VI.   Summary and Conclusions

The computational technology has sufficiently matured during the last two decades to justify revisiting and automating the sonic boom minimization problem. This paper reports on such an effort performed at the University of Colorado and focused on the constrained shape optimization of a supersonic aircraft for minimizing the ISPR. For this purpose, elements from the linearized sonic boom theory were combined with elements from the nonlinear aerodynamic theory, and a computational-based low-boom shaping methodology was developed. Even though it is based on the Whitham F function, this methodology operates directly on the geometry of the aircraft and addresses separately at each iteration of the optimization process the contributions of volume and lift. Each of its underlying design, analysis, and optimization models is equipped to address radical changes in both the geometry and the topology of the initial shape of an aircraft to reduce the ISPR, rather than small amplitude perturbations. Wings can be twisted, swept forward or backward, cranked, or even translated along the fuselage during the optimization process without requiring any intervention from the analyst or necessitating a remeshing of the geometry. This methodology was successfully applied to the shape optimization of LM's point of departure aircraft, and to some extent, to Reno Aeronautical's laminar-flow aircraft. Neglecting the effect of the propulsion system, a tenfold reduction in the ISPR on the ground was demonstrated for LM's supersonic design, from 1.623 psf (77.71 N/m^2) at $M_\infty = 1.5$ to 0.152 psf (7.278 N/m^2), while maintaining constant lift but increasing by 9% the combined induced and wave drag. This exercise revealed the expected result that the canard can increase the apparent bluntness of the equivalent body of revolution with a corresponding ISPR reduction. Tilting the aircraft nose, however, appears to have a minor effect on the sonic boom performance. The exact position of the canard relative to the nose of the aircraft also appears to have, at least in the case of LM's point of departure aircraft, a minor effect on sonic boom performance. On the other hand, this exercise clearly demonstrated that the dihedral, sweep, and twist angles of the wings and control surfaces can have a significant effect on sonic boom performance. It remains to investigate the influence of other parameters such as camber and to perform the constrained optimization of the fuselage.

Acknowledgments

References

[1] High Speed Civil Transport, *Program Review*, the Boeing Commercial Airplane Group, P.O. Box 3707, Seattle, WA 98124-2207.

[2] Petty, J. S., "Lower Bounds for Sonic Boom Considering the Negative Overpressure Region," *Journal of Aircraft*, Vol. 7, No. 4, July–Aug. 1970, pp. 375–377.

[3] Whitham, G. B., "The Flow Pattern of a Supersonic Projectile," *Communications on Pure and Applied Mathematics*, Vol. 5, No. 3, 1952, pp. 301–338.

[4] Lomax, H., "The Wave Drag of Arbitrary Configurations in Linearized Flow as Determined by Areas and Forces in Oblique Planes," NACA RM A55A18, 1955.

[5] Walkden, F., "The Shock Pattern of a Wing-Body Combination, Far from the Flight Path," *Aeronautical Quarterly*, Vol. 9, No. 2, 1958, pp. 164–194.

[6] Seebass, R., and Argrow, B., "Sonic Boom Minimization Revisited," AIAA Paper No. 98-2956, 1998.

[7] Mack, R. J., and Darden, C. M., "Wind Tunnel Investigation of the Validity of a Sonic-Boom-Minimization Concept," NASA TP 1421, 1979.

[8] Carlson, H. W., "Correlation of Sonic-Boom Theory with Wind-Tunnel and Flight Measurements," NASA TR R-213, 1964.

[9] Darden, C. M., "Sonic Boom Theory: Its Status in Prediction and Minimization," *Journal of Aircraft*, Vol. 129, No. 6, 1977, pp. 569–576.

[10] Carlson, H. W., Barger, R. L., and Mack, R. J., "Application of Sonic-Boom Minimization Concepts in Supersonic Transport Design," NASA TN D-7218, 1973.

[11] McLean, F. E., "Some Nonasymptotic Effects on the Sonic Boom of Large Airplanes," NASA TN D-2877, 1965.

[12] Hayes, W. D., and Haefeli, R. C., "The ARAP Sonic Boom Program," *Sonic Boom Workshop*, edited by I. A. Schwartz, SP-180, NASA, 1968, pp. 151–158.

[13] George, A. R., and Seebass, R., "Sonic Boom Minimization Including Both Front and Rear Shock Waves," *AIAA Journal*, Vol. 10, No. 10, 1969, pp. 2091–2093.

[14] Hayes, W. D., Haefeli, R. C., and Kulsrud, H. E., "Sonic Boom Propagation in a Stratified Atmosphere, with Computer Program," NASA CR-1299, 1969.

[15] Argrow, B., Farhat, C., Maute, K., and M. Nikbay, "Linear-Theory-Based Shape Optimization for Sonic Boom Minimization," *IUTAM Symposium Transsonnicum IV*, Goettingen, Germany, 2002.

[16] Darden, C. M., "Charts for Determining Potential Minimum Sonic Boom Overpressures for Supersonic Cruise Aircraft, NASA TN 1820, 1981.

[17] Yamaguchi, H., and Y. Nakamura, "Optimization of Low Boom Configuration of SST by Genetic Algorithm," AIAA Paper 98-2899, 1998.

[18] Maute, K., Nikbay, M., and Farhat, C., "Coupled Analytical Sensitivity Analysis and Optimization of Three-Dimensional Nonlinear Aeroelastic Systems," *AIAA Journal*, Vol. 39, No. 11, 2001, pp. 2051–2061.

[19] Jones, L. B., "Lower Bounds for Sonic Bangs," *Journal of the Royal Aeronautical Society*, Vol. 65, June 1961, pp. 433–436.

[20] Coen, P. G., "Development of a Computer Technique for the Prediction of Transport Aircraft Flight Profile Sonic Boom Signature," M.S. Thesis, George Washington University, Washington, D.C., 1991.

[21] Farhat, C., Geuzaine, P., and Brown, G., "Application of a Three-Field Nonlinear Fluid-Structure Formulation to the Prediction of the Aeroelastic Parameters of an F-16 Fighter," *Computers and Fluids*, Vol. 32, No. 1, Jan. 2003, pp. 3–29.

[22] Dervieux, A., "Steady Euler Simulations Using Unstructured Meshes," *Proceedings of the VKI Lectures Series* 1985-04, 16th Computational Fluid Dynamics, von Karman Institute, Brussels, Belgium, 1985.

[23] Cai, X. C., Farhat, C., and Sarkis, M., "A Minimum Overlap Restricted Additive Schwarz Preconditioner and Applications in 3D Flow Simulations," *The Tenth International Conference on Domain Decomposition Methods for Partial Differential Equations*, edited by C. Farhat, J. Mandel, and X.-C. Cai, AMS, Boulder, CO, 1998.

[24] Farhat, C., Degand, C., Koobus, B., and Lesoinne, M., "Torsional Springs for Two-Dimensional Dynamic Unstructured Fluid Meshes," *Computer Methods in Applied Mechanics and Engineering*, Vol. 163, Nos. 1–4, Sept. 1998, pp. 231–245.

[25] Degand, C., and Farhat, C., "A Three-Dimensional Torsional Spring Analogy Method for Unstructured Dynamic Meshes," *Computers and Structures*, Vol. 80, Nos. 3–4, Feb. 2002, pp. 305–316.

[26] Maute, K., Schwarz, S., and Ramm, E., "Structural Optimization—The Interaction Between Form and Mechanics," *Zeitschrift für Angewandte Mathematik und Mechanik*, Vol. 79, No. 10, 1999, pp. 651–673.

[27] Schittkowski, K., Zillober, C., and Zotemantel, R., "Numerical Comparison on Nonlinear Programming Algorithms for Structural Optimization," *Structural Optimization*, Vol. 7, No. 1, 1994, pp. 1–28.

[28] Lesoinne, M., Sarkis, M., Hetmaniuk, U., and Farhat, C., "A Linearized Method for the Frequency Analysis of Three-Dimensional Fluid/ Structure Interaction Problems in All Flow Regimes," *Computer Methods in Applied Mechanics and Engineering*, Vol. 190, Nos. 24–25, 2001, pp. 3121–3146.

M. Sichel
Associate Editor